

Supporting information

Voltage-controlled magnetic anisotropy gradient-driven skyrmion-based half-adder and full-adder

Sarwath Sara¹, Chandrasekhar Murapaka² and Arabinda Haldar^{1*}

¹Department of Physics, Indian Institute of Technology Hyderabad, Kandi, Sangareddy, Telangana 502284, India

²Department of Materials Science and Metallurgical Engineering, Indian Institute of Technology Hyderabad, Kandi 502285, Telangana, India

Corresponding authors: Electronic address: arabinda@phy.iith.ac.in

The file includes the following:

Supplementary Movie SV1. Skyrmion-based HA with 0-1 logic operation resulting in Sum as high and Carry as low state.

Supplementary Movie SV2. Skyrmion-based HA with 1-0 logic operation resulting in Sum as high and Carry as low state.

Supplementary Movie SV3. Skyrmion-based HA with 1-1 logic operation resulting in Sum as low and Carry as high state.

Supplementary Movie SV4. Skyrmion-based FA with 0-0-1 logic operation resulting in Sum as high and Carry as low state.

Supplementary Movie SV5. Skyrmion-based FA with 0-1-0 logic operation resulting in Sum as high and Carry as low state.

Supplementary Movie SV6. Skyrmion-based FA with 1-0-0 logic operation resulting in Sum as high and Carry as low state.

Supplementary Movie SV7. Skyrmion-based FA with 0-1-1 logic operation resulting in Sum as low and Carry as high state.

Supplementary Movie SV8. Skyrmion-based FA with 1-0-1 logic operation resulting in Sum as low and Carry as high state.

Supplementary Movie SV9. Skyrmion-based FA with 1-1-0 logic operation resulting in Sum as low and Carry as high state.

Supplementary Movie SV10. Skyrmion-based FA with 1-1-1 logic operation resulted in Sum and Carry being in a high state.

Fig. S1: Schematic with complete description of dimensions of HA and FA devices.

Fig. S2: Speed analysis of input A and input B skyrmions.

Fig. S3: Variation of the width of the devices to demonstrate flexibility.

Fig. S4: Changing the S output arm's position along the device's length to ensure reliability.

Fig. S5: Changing the S output arm's position along the device's width to ensure reliability.

Fig. S6: Variation of the angle between Input A and S output arm to examine the working of the devices for different values of α .

Fig. S7: Investigation of working of the devices for different notch sizes.

Fig. S8: Variation of notch geometry and dimensions.

Fig. S9: Gradual tapering of C_0 output arm.

Fig. S10: Determination of skyrmion velocity in nanotracks of various lengths.

Fig. S11: Cascading of the device.

Fig. S12: Determination of skyrmion's position along the length (x) of the device as a function of a critical time for different values of anisotropy gradient.

Fig. S13: Analyzing the effect of anisotropy gradient on the skyrmion size at input A and S output.

1. Schematic of skyrmion-based HA and FA:

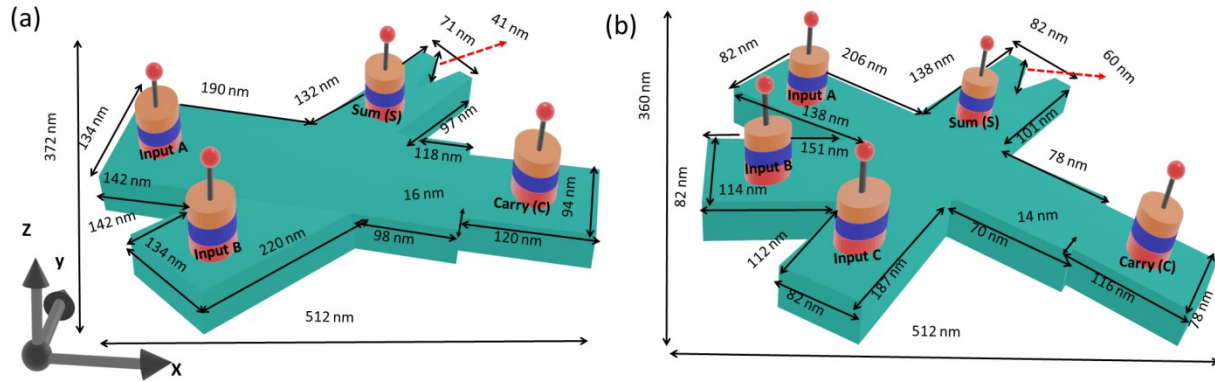


Fig. S1. Schematic of skyrmion-based logic device: (a) Half-adder with two inputs (A, B) and two outputs (S, C₀) (b) Full-adder with three inputs (A, B, C) and two outputs (S, C₀).

2. Skyrmion speed analysis:

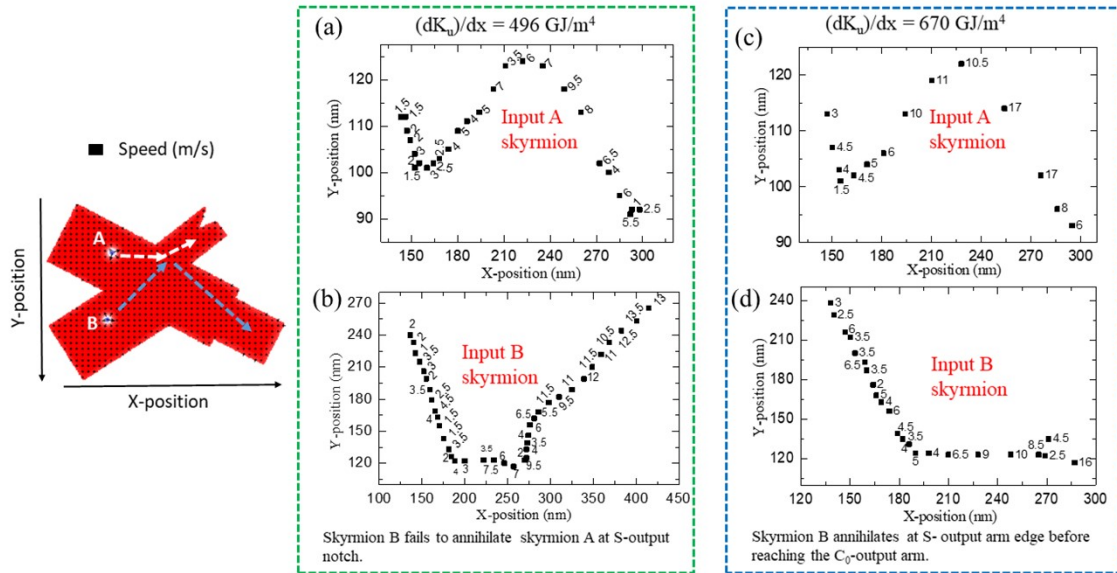


Fig. S2. Analysis of skyrmion's speed (m/s) at different positions of the device for anisotropy gradient of (i) 496 GJ/m⁴ (a) Input A skyrmion (b) Input B skyrmion (ii) 670 GJ/m⁴ (c) Input A skyrmion (d) Input B skyrmion.

Fig. S2 depicts the speed analysis of skyrmions A and B performed at various locations of the device and measured at every 1 ns for anisotropy gradients of 496 GJ/m⁴ and 670 GJ/m⁴. These values exceed the optimal anisotropy gradient, resulting in device failure. Skyrmion B drives skyrmion A towards the notch with a speed of 3.5 m/s, which is insufficient to annihilate the skyrmion A, and therefore the device fails. While the anisotropy gradient of 670 GJ/m⁴ results in a skyrmion B velocity of 10 m/s, this velocity annihilates skyrmion A at the notch. However, it annihilates at the edge of the S-output arm, resulting in device failure.

Robustness of geometry: 3. Variation of width:

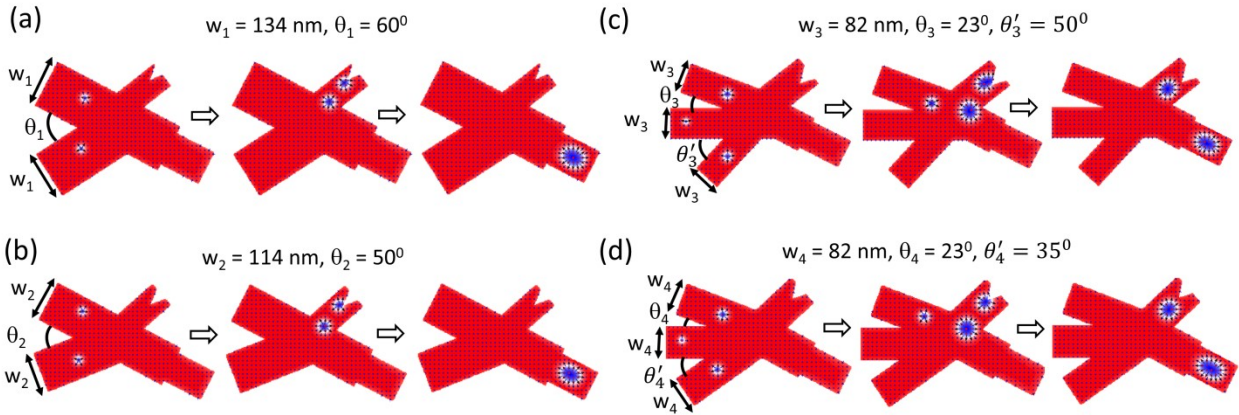


Fig. S3. Robustness of the geometry by variation of the width of the nano-device, altering the width of individual input regions and also the angle between them for HA (a) $w_1=134$ nm $\theta_1=60^\circ$ resulting in the total width of the device to be 170 nm (b) $w_2=114$ nm $\theta_2= 50^\circ$ resulting in total width of the device to be 130 nm, for FA (c) $w_3= 82$ nm $\theta_3= 23^\circ$, $\theta_3' = 50^\circ$ resulting in the total width of the device to be 360 nm (d) $w_3= 82$ nm $\theta_3= 23^\circ$, $\theta_3' = 35^\circ$ resulting in the total width of the device as 345 nm.

We have investigated the robustness of the device by varying the inputs' width and the angle between them. Fig.S3(a) represents the working of HA for $w_1= 134$ nm, $\theta_1= 60^\circ$, resulting in the device's total width of 170 nm. We have decreased the width to 130 nm by reducing the width of

inputs and the angle between them as $w_2=114$, nm $\theta_2= 50^0$, respectively, as indicated in Fig. S3(b); HA operates successfully. Similarly, we have realized the working of FA, retaining the constant width of inputs and the angle between input A and input B as 82 nm and 23^0 , respectively. We have changed the angle between input B and input C from 50^0 to 35^0 , which changes the device's total width from 360 nm to 345 nm, as shown in Fig. S3(c and d), respectively. We have observed a successful realization of both HA and FA logic functionalities, revealing the feasibility of the devices.

4. Variation of S output arm position along the x-axis:

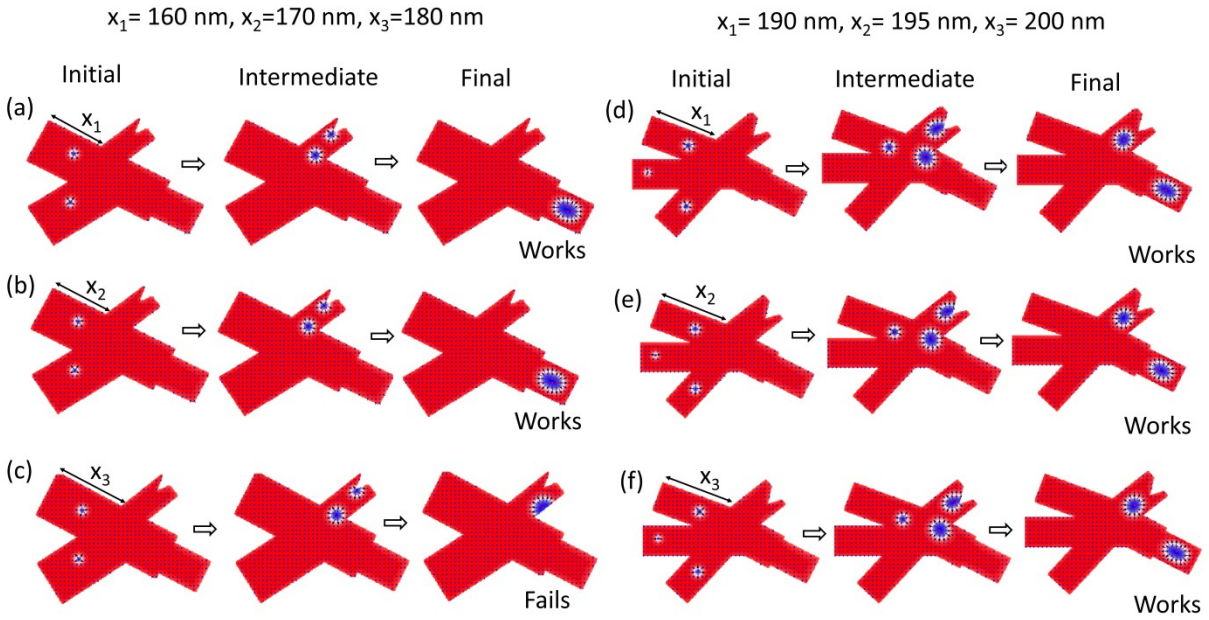


Fig. S4. Robustness of the geometry by varying the position of the S output arm along the x direction of the nano-device keeping constant length as 512 nm and width 370nm for HA (a) $x_1=160$ nm (b) $x_2= 170$ nm (c) $x_3= 180$ nm and for FA length as 512 nm and width as 360 nm (d) $x_1=190$ nm (e) $x_2= 195$ nm (f) $x_3= 200$ nm.

Next, the S output arm's position is varied along the device's x-axis, keeping length and width constant as 512 nm, 370 nm for HA, 512 nm, and 360 nm for FA, respectively. For HA, the S

output arm's position is varied as $x_1=160$, $x_2=170$, and $x_3=180$ nm; for x_1 and x_2 , the device works as indicated in Fig. S4(a and b), respectively. For x_3 , the edge repulsions from the tilted edge at the S output arm dominate the other forces and result in the annihilation of input B skyrmion before reaching the C_0 output. Hence, HA fails to operate for 180 nm. However, FA works for all $x_1=190$, $x_2=195$, and $x_3=200$ nm, as indicated in Fig. S4(d-f).

5. Variation of S output arm position along the y-axis:

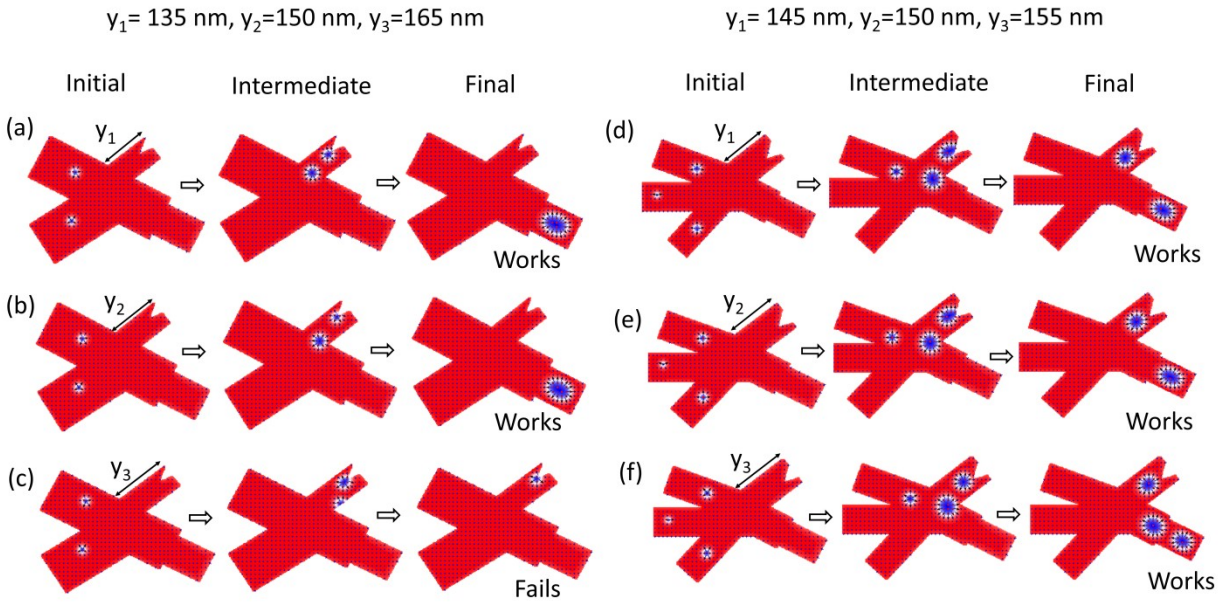


Fig. S5. Robustness of the device by varying the position of the Sum output arm along the y -direction of the nano-device keeping constant length as 512 nm and width 370nm for HA (a) $y_1=135$ nm (b) $y_2 = 150$ nm (c) $y_3 = 165$ nm and for FA length as 512 nm and width as 360 nm (d) $y_1=145$ nm (e) $y_2 = 150$ nm (f) $y_3 = 155$ nm.

We analyze the working of the devices varying the S output arm's position along the y -axis of the device for fixed values of length and width of HA as 512 nm and 370 nm, respectively, and for FA 512 nm and 360 nm, respectively. The device works precisely for HA with $y_1=135$ nm and $y_2 =150$ nm, while it fails for $y_3=165$ nm, as shown in Fig. S5(a-c). For 165 nm, the input A

skyrmion travels a greater distance into the S output arm, allowing the input B skyrmion to occupy the S output arm. Subsequently, mutual repulsive force pushes them away from each other, resulting in the annihilation of the input A skyrmion. In contrast, the input B skyrmion annihilates being pushed towards the tilted edge of the S output arm and does not reach the C_0 output. For the other cases, the input A skyrmion stops the input B skyrmion from entering into the S output arm and diverges it towards the C_0 output. Now, we discuss FA operation; the case with 155 nm is exceptional but still works. Primarily, the input A skyrmion occupies the S output arm, and then the input C skyrmion arrives at the doorstep of the S output arm. The skyrmions push away each other, resulting in the input C skyrmion deflecting towards the C_0 output. Still, the skyrmion at the S output arm does not annihilate at the notch due to the increased dimension of the S output arm. The input B skyrmion also fails to annihilate the input A skyrmion and deflects toward the C_0 output, resulting in two skyrmions at the C_0 output. The device works precisely at 145 and 150 nm, as shown in Fig. 5(d-f).

6. variation of the angle between input A and S output arms:

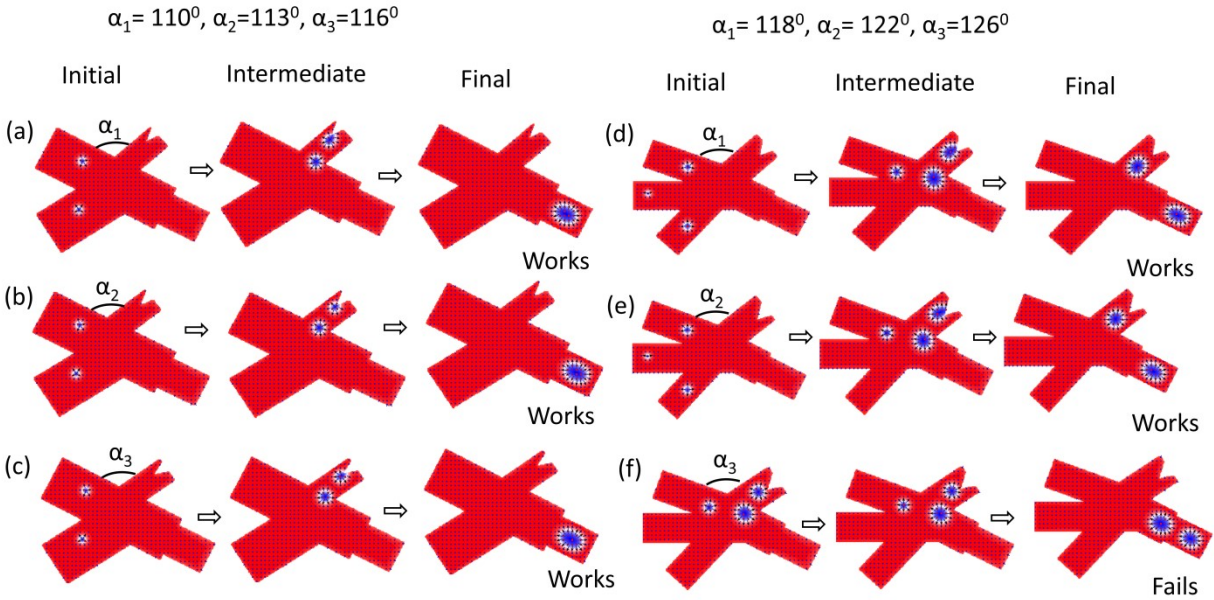


Fig.S6. Robustness of the geometry by varying the angle between input A region and S output region of the nano-device keeping constant length as 512 nm and width 370nm for HA (a) $\alpha_1=110^\circ$ (b) $\alpha_2 = 113^\circ$ (c) $\alpha_3 = 116^\circ$ nm and for FA length as 512 nm and width as 360 nm (d) $\alpha_1=118^\circ$ (e) $\alpha_2 = 122^\circ$ (f) $\alpha_3 = 126^\circ$.

To further examine the robustness of the devices, the angle between the input A and the S output arms is varied. HA logic functionality is realized for different angles, such as 110° , 113° , and 116° , as shown in Fig. S6(a-c). At the same time, the FA device works for 118° and 122° and fails to operate at 126° , as shown in Fig. S6(d-f). For 126° , the input C skyrmion experiences a more prominent force from the tilted edge at the S output arm and exerts a less repulsive force on the input A skyrmion present at S. As a result, input C skyrmion is unsuccessful in annihilating the input A skyrmion at the notch and deflects towards the C_0 output as indicated in the intermediate state of Fig. S6(f). While the input B skyrmion arrives, the S output arm experiences a similar mechanism but annihilates the input A skyrmion at a notch while moving

toward the C_0 output. As a result, we find no skyrmion at the S output and two at the C_0 output as the final read-out operation, violating the FA logic functionality.

7. Variation of notch size:

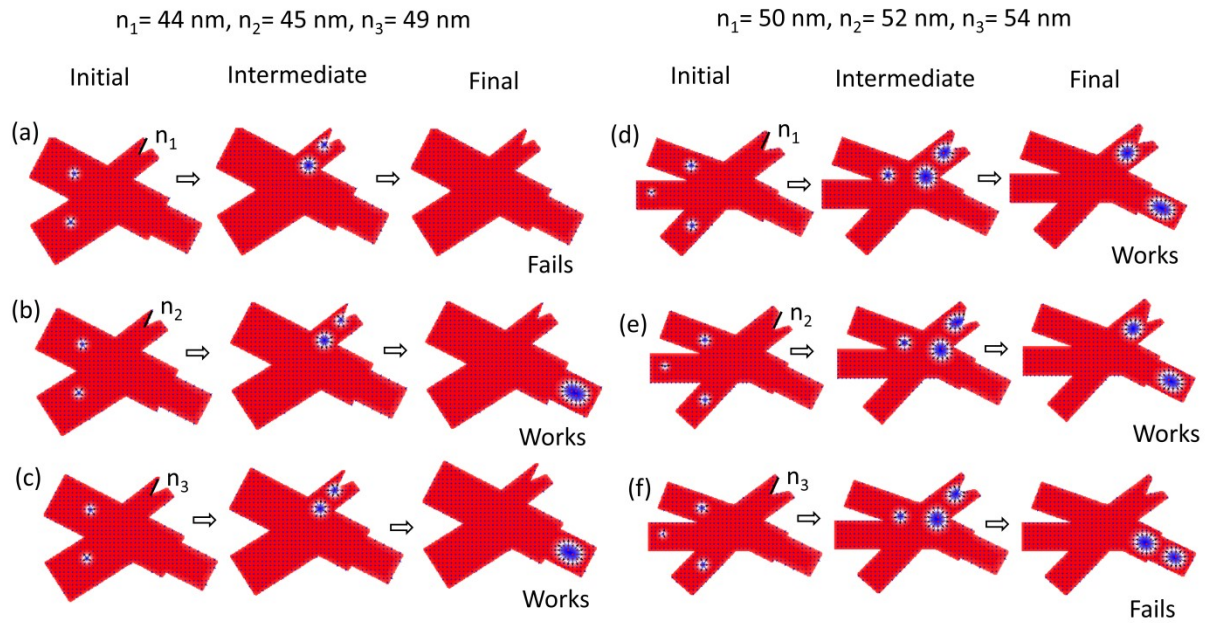


Fig. S7. Robustness of the geometry by varying the size of the notch present in the S output region of the nano-device keeping constant length as 512 nm and width 370nm for HA (a) $n_1=44$ nm (b) $n_2=45$ nm (c) $n_3=49$ nm and for FA length as 512 nm and width as 360 nm (d) $n_1=50$ nm (e) $n_2=52$ nm (f) $n_3=54$ nm.

Next, HA's notch size is varied to 44, 45, and 49 nm; logic functionality is achieved for 45 and 49 nm and fails for 44 nm, as shown in Fig. S7(a-c). For 44 nm notch size, the input A skyrmion moves closer to the edge of the arm due to the smaller notch size and welcomes the input B skyrmion into the S output arm. The mutual repulsions push them away from each other and input A skyrmion annihilates at the notch, deflecting input B skyrmion towards the tiled edge of the S output arm. The input B skyrmion annihilates at the tilted edge; we end up with no skyrmion at the output states and fail to achieve HA logic functionality. The FA logic

functionality is realized for 50 and 52-nm notch sizes as indicated in Fig. S7(d & e) and fails to operate at 54 nm following the same physical mechanism discussed in Fig. S6(f).

8. Variation of notch dimensions and geometry:

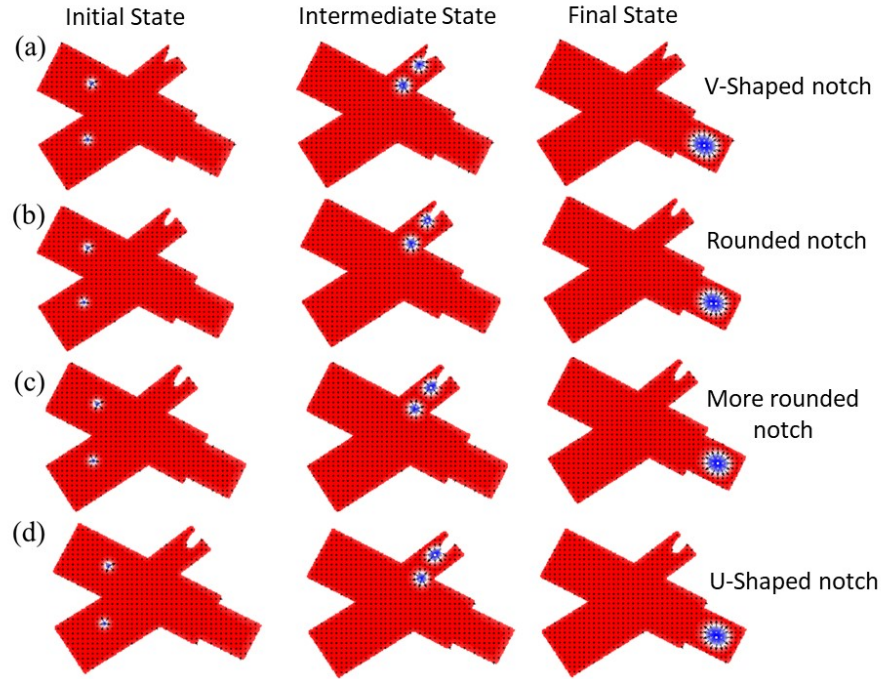


Fig. S8. Variation of shape and size of notch (a) triangular notch, elliptical notches of minor axis (b) 11 nm (c) 13 nm (d) 15 nm.

The impacts of varying the notch dimensions and geometry are shown in Fig. S8. This study's notch is rounded instead of the pointed tip, considering the deviations expected in the nanofabrication processes. Fig. S8 shows that changing the triangular region to an elliptical shape doesn't affect the logic operations. The notch geometry is altered from a V-shape to a U-shape to examine the device's operation. The successful operation is demonstrated when an ellipsoid minor axis is changed from 11 nm to 15 nm to make the notch more rounded to account for the slight deviation expected in the nanofabrication.

9. Gradual tapering of C_0 output arm:

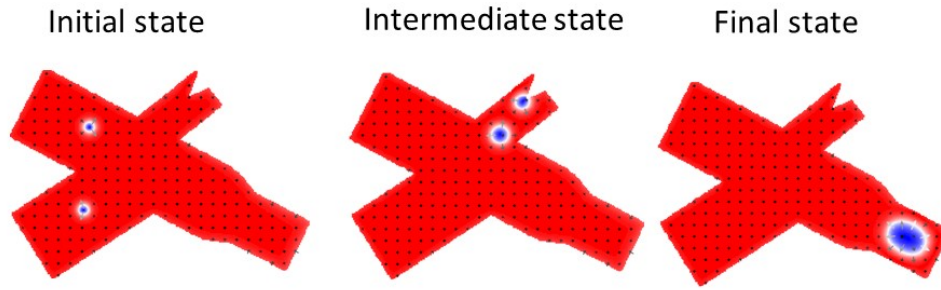


Fig. S9. Gradual tapering of the C_0 output region arm.

Fig. S9 represents the successful operation of the device for gradual tapering of C_0 output instead of a sharp step considering the deviations expected in nanofabrication processes based on lithographic techniques.

10. Speed of skyrmion in various nanotracks of different lengths:

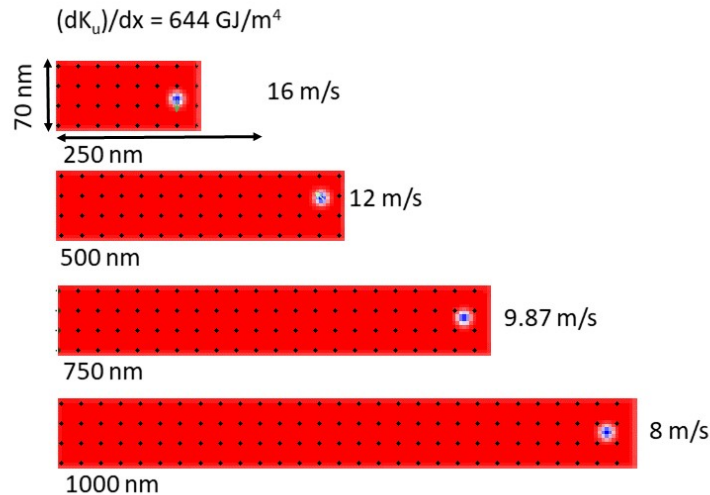


Fig. S10. The velocity of skyrmions in the 70-nm-wide nanotracks with different lengths (a) 250 nm, (b) 500 nm, (c) 750 nm, and (d) 1000 nm. The magnetic anisotropy gradient was set to 644 GJ/m^4 .

We have conducted additional simulations to analyze the maximum distance the skyrmion can travel. In this regard, we have designed a 70-nm-wide nanotrack with various lengths: 250, 500,

750, and 1000 nm, as shown in Fig. S10. We have found that the skyrmion can travel long distances without deforming or annihilating when the VCMA gradient is constant (644 GJ/m^4). However, the velocity drops from 16 m/s to 8 m/s when the length is increased from 250 to 1000 nm. One can utilize larger anisotropy gradients to achieve higher skyrmion velocity. We have changed this magnetic anisotropy gradient along a $500 \times 70 \text{ nm}^2$ nanotrack in order to evaluate its range. Note that the skyrmion size becomes larger and eventually deforms when the anisotropy gradient increases. Therefore, the skyrmion cannot be stabilized beyond a specific limit of the magnetic anisotropy K_u . This can constrain the skyrmion's velocity but not its range of travel.

11. Cascading:

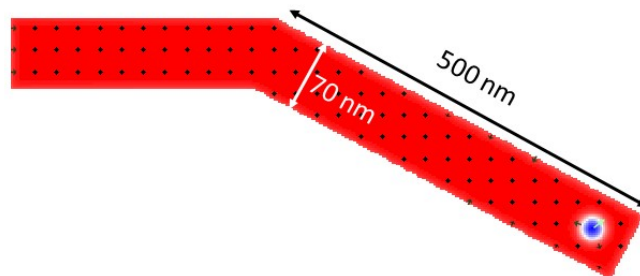


Fig. S11. Skyrmion in an elongated nanotrack to facilitate cascading.

In order to study the cascading of the logic device, we created a device with an elongated output arm that is 500 nm long and 70 nm wide. As shown in Fig. S11, the skyrmion successfully reaches the other end of the output arm. The above findings (Fig. S10-S11) demonstrate the scope of our device architecture for potential cascading and fanout operation.

12. The behavior of skyrmion at the notch:

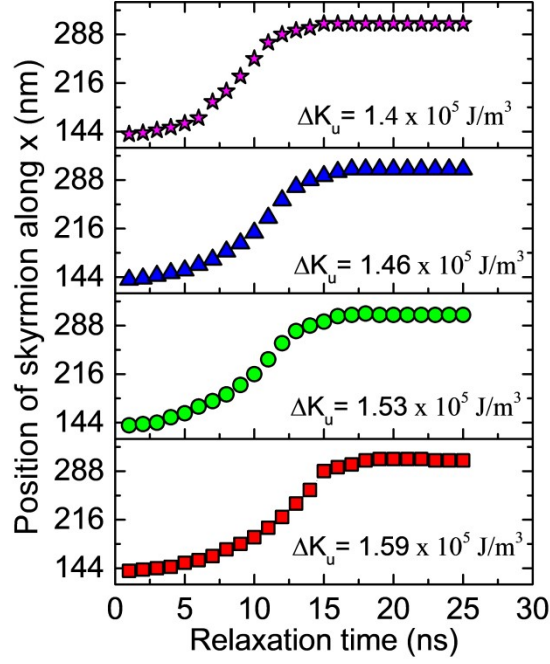


Fig. S12. The behavior of the skyrmion at the notch present in the S output of HA, the position of the skyrmion along the length (x) of the device as a function of relaxation time for different values of anisotropy gradient.

The skyrmion trajectory as a function of critical time (time taken by the skyrmion to reach the S output after injecting them at the inputs) is tracked during its motion towards the S output, as shown in Fig. S12. The magnitude of vector force \vec{F} arise due to the inhomogeneous distribution of magnetic anisotropy energy generated using VCMA given by

$$F_{(vcma)} = - \frac{\partial E_{K_u}}{\partial K_u} \frac{\partial K_u}{\partial x} \quad (1)$$

$$E_{K_u} = - K_u (m.z)^2 \pi R_{sk}^2 d \quad (2)$$

Equation (2) indicates the dependency of E_{K_u} on skyrmion size, and equation (1) shows the influence of E_{K_u} on $F_{(vcma)}$. As the values of ΔK_u increase, the skyrmion size also increases, which increases E_{K_u} and hence the VCMA gradient force. Consequently, the VCMA gradient favors and exerts a stronger force on larger skyrmions, resulting in higher skyrmion velocity.¹ Therefore, the skyrmion stabilizes in the S output in a shorter critical time for higher anisotropy gradient values.

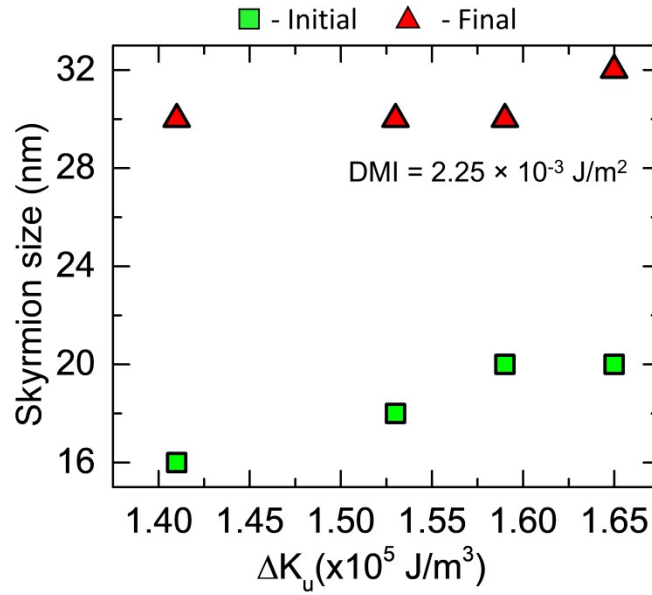


Fig. S13. The effect of anisotropy gradient on the size of the skyrmion at input A and S output is recorded for different values of anisotropy gradient.

The magnetic anisotropy also determines the size of the skyrmions, which is a critical parameter to address the reliable operation of the logic device. Fig. S13 shows the skyrmion size at input A (initial) and S output (final) positions. Initially, skyrmion acquires a size of 16, 18, 20, and 20 nm for ΔK_u 1.41×10^5 , 1.53×10^5 , 1.59×10^5 , and 1.65×10^5 J/m³ respectively, and acquires a size of

30 nm reaching the S output region for 1.41×10^5 , 1.53×10^5 , 1.59×10^5 J /m³, and 32 nm for 1.65×10^5 J/m³ while the DMI is kept constant at 2.25×10^{-3} J/m².

References:

- 1 X. Wang, W. L. Gan, J. C. Martinez, F. N. Tan, M. B. A. Jalil and W. S. Lew, *Nanoscale*, 2018, **10**, 733–740.